Title

A framework for synthetic validation of 3D echocardiographic particle image velocimetry

Journal

Meccanica, 52(3)

ISSN

0025-6455

Authors

Falahatpisheh, Ahmad

Kheradvar, Arash

Publication Date

2017-02-01

DOI

10.1007/s11012-015-0342-6

Peer reviewed

Meccanica
DOI 10.1007/s11012-015-0342-6

A framework for synthetic validation of 3D echocardiographic particle image velocimetry

Ahmad Falahatpisheh · Arash Kheradvar

Received: 16 August 2015 / Accepted: 1 December 2015

Abstract Particle image velocimetry (PIV) has been significantly advanced since its conception in early 1990s. With the advancement of imaging modalities, applications of 2D PIV have far expanded into biology and medicine. One example is echocardiographic particle image velocimetry that is used for in vivo mapping of the flow inside the heart chambers with opaque boundaries. Velocimetry methods can help better understanding the biomechanical problems. The current trend is to develop three-dimensional velocimetry techniques that take advantage of modern medical imaging tools. This study provides a novel framework for validation of velocimetry methods that are inherently three dimensional such as but not limited to those acquired by 3D echocardiography machines. This framework creates 3D synthetic fields based on a known 3D velocity field **V** and a given 3D brightness field **B**. The method begins with computing the inverse flow $\mathbf{V}^*$ based on the velocity field **V**. Then the transformation of **B**, imposed by **V**, is calculated using the computed inverse flow according to $\mathbf{B}^*(\mathbf{x}) = \mathbf{B}(\mathbf{x} + \mathbf{V}^*(\mathbf{x}))$, where **x** is the coordinates of voxels in $\mathbf{B}^*$, with a 3D weighted average interpolation, which provides high accuracy, low memory requirement, and low computational time. To check the validity of the framework, we generate pairs of 3D brightness fields by employing Hill's spherical vortex velocity field. **B** and the generated $\mathbf{B}^*$ are then processed by our in-house 3D particle image velocimetry software to obtain the interrelated velocity field. The results indicates that the computed and imposed velocity fields are in agreement.

Keywords Particle image velocimetry · Hill's spherical vortex · Echocardiography · Brightness field · Echo-PIV

1 Introduction

The most commonly used velocimetry techniques to measure optical flows are based on tracing the particles in a fluid flow. Since early 1990s, several algorithms for particle tracking have been developed that are generally referred to as particle image velocimetry (PIV). PIV techniques were originally developed based on the snapshots of two- or three-component velocity vector field on a planar cross-section of the flow [1]. PIV techniques have been evolving with the advancement of software technology, the birth of faster processors, and the technical improvements in imaging hardware. These new advances facilitate the development of new modalities for measuring the velocity over volumetric domains.

A. Falahatpisheh · A. Kheradvar (✉)
Department of Biomedical Engineering, Edwards Lifesciences Center for Advanced Cardiovascular Engineering, University of California, Irvine, 2410 Engineering Hall, Irvine, CA 92697, USA
e-mail: arashkh@uci.edu

Published online: 22 December 2015

Therefore, there is a need for a platform to systematically validate new methods.

Some of the noteworthy three-dimensional PIV techniques are Defocusing PIV (DDPIV) [2], Holographic PIV [3], Multi-Planar PIV [4], and Tomographic PIV [5]. The accuracy of the measurement for each 3D PIV method depends on many experimental parameters, particularly on particle image density, volume depth, and type and number of acquisition devices, which make quantitative validation challenging [6, 7]. However, while the three-dimensional velocity in a particular flow situation is unique, it is anticipated that each 3D PIV technique reports a slightly different vector fields. In that regards, there are currently few benchmarks available for validation of 3D PIV systems that use multiple cameras [6].

Recent innovations in echocardiography have launched new venues for novel PIV techniques. Currently, modern echocardiography systems are equipped with ultrasound probes that can capture three dimensional particle brightness fields associated with the blood flow in cardiovascular system. They use ultrasound contrast agents, or even blood components to image the flow. These new advancements may overcome the existing limitations in characterizing the cardiac flows [8–13].

The flow data acquired by modern echocardiography systems has a distinct feature compared to the conventional 3D PIV setups. Echocardiography's matrix-array probes provide three dimensional datasets in VolDICOM[1] format that includes all the information about brightness field and exact 3D location of each fluid tracer, $B(x, y, z, t)$. In contrast to VolDICOM data, the images acquired by conventional 3D PIV systems are 2D images obtained from more than one camera, and reconstructed according to the PIV modality (e.g., DDPIV, tomographic PIV, etc). Accordingly, the frameworks that are aimed to process 3D echocardiographic datasets require validation. This can be done by processing two physically-interrelated known particle fields whose relation is defined by a known 3D velocity field. The present work describes a method to reconstruct a physically-interrelated pair of synthetic three dimensional particle fields according to a known velocity vector field.

[1] Volumetric Digital Imaging and Communications in Medicine.

2 Methods

Generating synthetic three dimensional dataset for validation of volumetric particle image velocimetry starts with creation of two consecutive volumetric frames, $\mathbf{B}(\mathbf{x})$ and $\mathbf{B}^*(\mathbf{x})$, where $\mathbf{x} = (x, y, z)$, and $\mathbf{B}$ and $\mathbf{B}^*$ are grayscale three dimensional brightness fields. Our approach is to transform the first randomly generated volumetric frame, $\mathbf{B}(\mathbf{x})$, using a known velocity field, $\mathbf{V}(\mathbf{x})$, to obtain the second volumetric frame, $\mathbf{B}^*(\mathbf{x})$. In fact, $\mathbf{V}(\mathbf{x})$ establishes the relation between the voxels of the two frames, as shown in Fig. 1. Furthermore, $\mathbf{V}(\mathbf{x})$ is considered to be a dense mapping in such a way that for each voxel in $\mathbf{B}$, there is

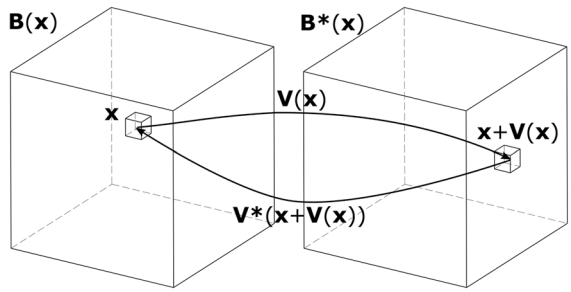

Fig. 1 Mapping of the voxel in the forward and inverse flows, $\mathbf{V}(\mathbf{x})$ and $\mathbf{V}^*(\mathbf{x})$, respectively

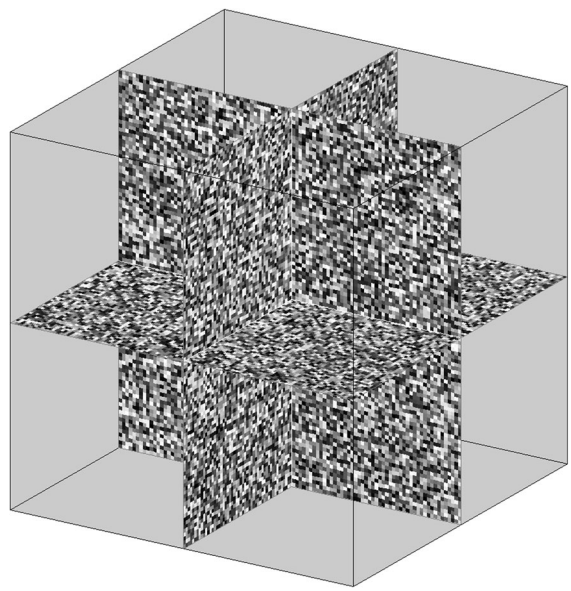

Fig. 2 Random brightness field, $\mathbf{B}(\mathbf{x})$. Three distribution of brightness is illustrated in three planes

a mapping for its corresponding voxel in $\mathbf{B}^*$. The process is initiated by populating a randomly distributed, three dimensional grayscale brightness field into $\mathbf{B}(\mathbf{x})$, a structured array of size M × N × K, with random numbers in the range of 0–255, as illustrated in Fig. 2.

Suppose $\mathbf{V}(\mathbf{x}) = (u(\mathbf{x}), v(\mathbf{x}), w(\mathbf{x}))$ is the forward flow, with $u(\mathbf{x})$, $v(\mathbf{x})$, $w(\mathbf{x})$, as the horizontal, vertical, and depth velocities in each voxel $\mathbf{x}$, respectively, where $\mathbf{x}$ is the coordinates of voxels in $\mathbf{B}$. The relation between the frames and the forward flow is:

$$\mathbf{B}(\mathbf{x}) = \mathbf{B}^*(\mathbf{x} + \mathbf{V}(\mathbf{x})) \tag{1}$$

Therefore, to compute $\mathbf{B}^*(\mathbf{x})$, the value of each pixel $\mathbf{B}(\mathbf{x})$ should be copied to the location $\mathbf{x} + \mathbf{V}(\mathbf{x})$ in $\mathbf{B}^*$. However, since the value of $\mathbf{V}(\mathbf{x})$ is in float precision, the position $\mathbf{x} + \mathbf{V}(\mathbf{x})$ does not coincide with the voxel grid. Here, we computed the inverse flow, $\mathbf{V}^*(\mathbf{x})$, instead of the forward flow, and used the following relation to create the second frame, as shown in Fig. 1. This is mainly done due to the ease of computer implementation, less memory usage, and low computational time.

$$\mathbf{B}^*(\mathbf{x}) = \mathbf{B}(\mathbf{x} + \mathbf{V}^*(\mathbf{x})) \tag{2}$$

where $\mathbf{x}$ is the coordinates of voxels in $\mathbf{B}^*$. Accordingly, the problem becomes the computation of the inverse optical flow:

$$\mathbf{V}^* = inv(\mathbf{V}) \tag{3}$$

We used an interpolation algorithm to find $\mathbf{V}^*$, as described by Sanchez et al. [14], and extended the methodology to three dimensional datasets. In fact, $\mathbf{V}^*(\mathbf{x})$ maps the voxels in the second frame to the voxels in the first frame. Since the volumetric frames are discrete 3D datasets, correspondence of each voxel in the first frame may lie among several voxels in the second frame, instead of perfectly lying on the grid nodes, and therefore, a weighted average was used to address this:

$$\mathbf{V}^*(\mathbf{x}) = -\frac{\sum_{\mathbf{x}_i \in N_i} w_i \mathbf{V}(\mathbf{x}_i)}{\sum_{\mathbf{x}_i \in N_i} w_i} \tag{4}$$

where $N_i \equiv \{\mathbf{x}_i : ||\mathbf{x}_i + \mathbf{V}(\mathbf{x}_i) - \mathbf{x}|| < 1\}$, i.e., the set of correspondences that lie around $\mathbf{x}$. The weights in the pseudocode above are illustrated in Fig. 3, where each weight represents the corresponding cell volume. Equation 4 was iteratively calculated to find the new value for a specific voxel. The algorithm was implemented in MATLAB (MathWorks, Natick, MA), as described in pseudocode 1 and 2.

Pseudocode 1 AVG(d, $\mathbf{V}$, $wght$, d^*, $\mathbf{V}^*$, $wght^*$)

```
if wght ≥ 0.125 then
  if abs( d - d* ) ≤ MOTION_TH then
    V* ← V* + V · wght
    wght* ← wght*+wght
  else if d ≥ d* then
    d* ← d
    V* ← V· wght
    wght* ← wght
  end
end
```

Pseudocode 2 Inverse Average Flow

Input: $\mathbf{V}$
Output: $\mathbf{V}^*$

Initialize buffers d^*, **avg_V**, $wght^*$ to 0

foreach *position* $\mathbf{x}$ **do**
  $\mathbf{x}_w \leftarrow \mathbf{x} + \mathbf{V}(\mathbf{x})$
  Find the eight neighbors of
    $\mathbf{x}_w : \{\mathbf{x}_1, \mathbf{x}_2, \mathbf{x}_3, \mathbf{x}_4, \mathbf{x}_5, \mathbf{x}_6, \mathbf{x}_7, \mathbf{x}_8\}$ (see Figure 3A)
  Compute the interpolation weights:
    $w_1, w_2, w_3, w_4, w_5, w_6, w_7, w_8$ (see Figure 3B)
  $d \leftarrow \|\mathbf{V}(\mathbf{x})\|^2$
  AVG (d, $\mathbf{V}(\mathbf{x})$, w_1, $d^*(\mathbf{x}_1)$, **avg_V**$(\mathbf{x}_1)$, $wght^*(\mathbf{x}_1)$)
  AVG (d, $\mathbf{V}(\mathbf{x})$, w_2, $d^*(\mathbf{x}_2)$, **avg_V**$(\mathbf{x}_2)$, $wght^*(\mathbf{x}_2)$)
  AVG (d, $\mathbf{V}(\mathbf{x})$, w_3, $d^*(\mathbf{x}_3)$, **avg_V**$(\mathbf{x}_3)$, $wght^*(\mathbf{x}_3)$)
  AVG (d, $\mathbf{V}(\mathbf{x})$, w_4, $d^*(\mathbf{x}_4)$, **avg_V**$(\mathbf{x}_4)$, $wght^*(\mathbf{x}_4)$)
  AVG (d, $\mathbf{V}(\mathbf{x})$, w_5, $d^*(\mathbf{x}_5)$, **avg_V**$(\mathbf{x}_5)$, $wght^*(\mathbf{x}_5)$)
  AVG (d, $\mathbf{V}(\mathbf{x})$, w_6, $d^*(\mathbf{x}_6)$, **avg_V**$(\mathbf{x}_6)$, $wght^*(\mathbf{x}_6)$)
  AVG (d, $\mathbf{V}(\mathbf{x})$, w_7, $d^*(\mathbf{x}_7)$, **avg_V**$(\mathbf{x}_7)$, $wght^*(\mathbf{x}_7)$)
  AVG (d, $\mathbf{V}(\mathbf{x})$, w_8, $d^*(\mathbf{x}_8)$, **avg_V**$(\mathbf{x}_8)$, $wght^*(\mathbf{x}_8)$)
end

foreach *position* $\mathbf{x}$ **do**
  $\mathbf{V}^*(\mathbf{x}) \leftarrow -\frac{\mathbf{avg\_V}(\mathbf{x})}{wght^*(\mathbf{x})}$
end

3 Results and discussion

3.1 Generation of interrelated brightness fields

We used the above-mentioned pseudocodes to create two brightness fields in three dimensions representing the Hill's spherical vortex (HSV). This vortex is an extreme member of the Norbury family of vortex rings [15], and is employed as a model in many applications

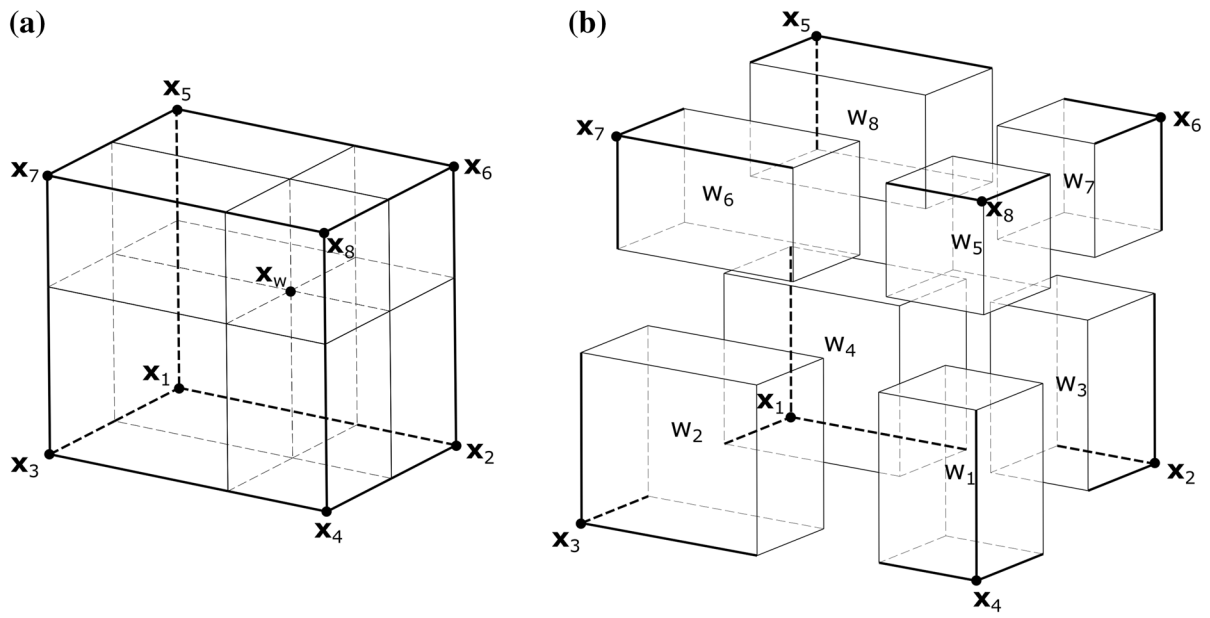

Fig. 3 Weights. **a** The eight nearest neighbors of point $\mathbf{x}_w$. **b** Illustrates the weights in Eq. 4, where each cell is isolated from its location in (**a**) for clarification purposes. Weights are the volume of each cell

such as the motion of droplets and bubbles at a high Reynolds number and for 3D PIV applications [4]. The vorticity inside the HSV is a linear function of the distance from the axis of symmetry. In an HSV, the internal flow has an axisymmetric vorticity distribution whereas the external flow is irrotational around a sphere.

An HSV is specified by the Stokes (axisymmetric) streamfunction as:

$$\psi = \begin{cases} \frac{3}{4} V_e r^2 \left(1 + \frac{\rho^2}{R^2}\right) & \rho^2 \leq R^2 (internal\,flow) \\ \frac{3}{4} V_e r^2 \left(\frac{R^3}{\rho^3} - 1\right) & \rho^2 \geq R^2 (external\,flow) \end{cases} \tag{5}$$

where R specifies the size of the spherical vortex, V_e is the external uniform vertical velocity; $r = \sqrt{x^2 + y^2}$ and $\rho = \sqrt{r^2 + z^2}$ are the cylindrical and spherical radial coordinates, respectively. The velocity field in Cartesian coordinates is computed by the streamfunction as:

$$u = -\frac{x}{r^2}\frac{\partial \psi}{\partial z}; \quad v = -\frac{y}{r^2}\frac{\partial \psi}{\partial z}; \quad w = \frac{1}{r}\frac{\partial \psi}{\partial r} \tag{6}$$

3.2 Transforming velocity field

We created a 3D HSV velocity field, $\mathbf{V}(u(\mathbf{x}), v(\mathbf{x}), w(\mathbf{x}))$, with a resolution of $100 \times 100 \times 100$ and unit radius and external velocity based on Eqs. 5 and 6. This velocity field was used to transform $\mathbf{B}$ into $\mathbf{B}^*$ based on the algorithm described earlier in the Sect. 2.

3.3 Validating the framework using an exemplary volumetric PIV method

$\mathbf{B}$ and $\mathbf{B}^*$ were accordingly processed by using an in-house Volumetric Echocardiographic Particle Image Velocimetry (V-Echo-PIV) software [16]. This software works based on iterative hierarchical PIV method to find the velocity vector fields. Here, we used our software for validation of the synthetic framework, and to examine whether it can obtain the velocity field corresponding to $\mathbf{B}$ and $\mathbf{B}^*$, in this case, an HSV velocity field. Furthermore, we added Gaussian noise to the second frame, $\mathbf{B}^*$, to investigate how noise can adversely affect the velocity measurements. The level of noise was determined according to the signal-to-noise ratio (SNR). We considered 1, 2, 5, 10,

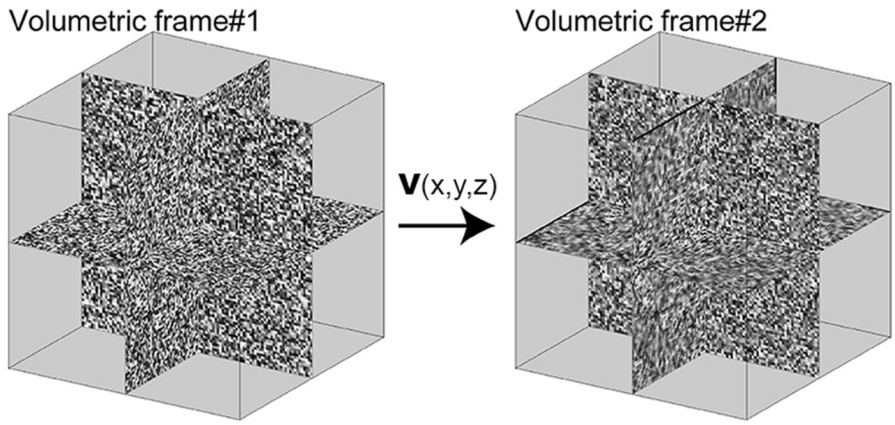

Fig. 4 Synthetic brightness field (Volumetric frame #2) generated using the random brightness field (Volumetric frame #1) in Fig. 2

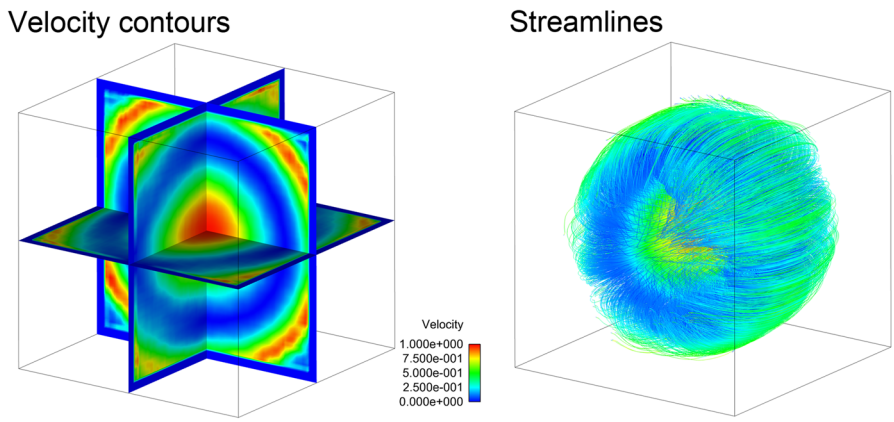

Fig. 5 Velocity contours and streamlines of Hill's spherical vortex obtained by V-Echo-PIV using the datasets in Fig. 4

15, 25, 50, and 100 dB for SNR. The noise was added during the processing of $\mathbf{B}$ and $\mathbf{B}^*$. We used three levels of hierarchy, i.e., coarsening and refining, as well as three different levels of iterations for each SNR in finding the velocity field. The root mean square (RMS) error, reported here as a function of the signal to noise ratio, level of hierarchy, and number of iterations, statistically represents the difference between the analytical HSV and the computed velocity field using $\mathbf{B}$ and $\mathbf{B}^*$:

$$Err_{\mathrm{RMS}} = \frac{\sqrt{\frac{1}{n}\sum\left[\left(u_{HSV}-u_{Comp}\right)^2+\left(v_{HSV}-v_{Comp}\right)^2+\left(w_{HSV}-w_{Comp}\right)^2\right]}}{V_{scale}} \tag{7}$$

where n is the resolution of the three dimensional domain, subscript *HSV* refers to the analytical *HSV* and subscript *Comp* represents the computed velocity component and V_{scale} is unity for the created HSV.

Figure 4 illustrates the two volumetric brightness fields that were generated according to the velocity field that defines Hill's spherical vortex. Three perpendicular slices of each frame are shown in Fig. 4. As can be seen, the corresponding slice is warped according to the given velocity $\mathbf{V}(\mathbf{x})$ and

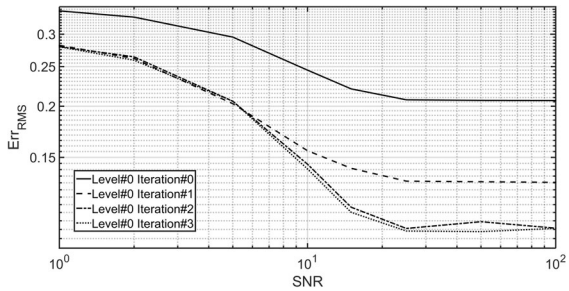

Fig. 6 The effect of the number of iterations, i.e., the number of times velocity was corrected, on the RMS error. In this figure, PIV implementation was non-hierarchical. Convergency was reached when velocity was corrected three times, which implies the computed velocity field by V-Echo-PIV reached to a minimum deviation from the analytical solution of the Hill's spherical vortex

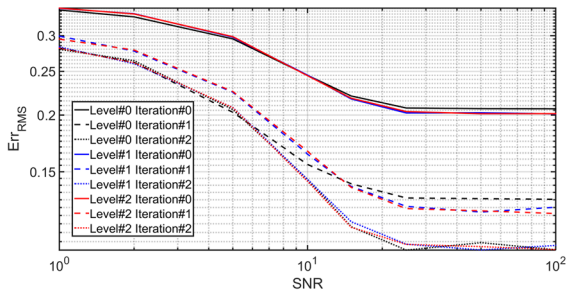

Fig. 7 The effects of hierarchical PIV, the number of iterations for correcting the velocity, and signal to noise ratio on the RMS error. Hierarchical PIV is shown by the number of levels in the figure. Level #0 means no hierarchical implementation and level #2 represents two level hierarchical PIV

implementing pseudocodes 1 and 2. **B** and $\mathbf{B}^*$ were then processed by V-Echo-PIV 3D velocimetry code. The velocity contours and streamlines associated with transformation of **B** to $\mathbf{B}^*$ are illustrated in Fig. 5. Figures 6 and 7 show how hierarchical PIV, number of iterations for velocity correction, and signal-to-noise ratio affect the RMS error. For level 0, where there was no coarsening and refining, convergency was achieved when velocity was corrected three times, with a slight difference in RMS error compared to using two-time velocity correction (two-time iterations). Accordingly, we inferred that additional iterations in our software improve the RMS error, bringing the results in better agreement with the analytical HSV. It was also observed that regardless of the number of levels, i.e., how many times the 3D dataset coarsened and refined, velocity correction significantly enhanced the results depending on the value of SNR. In other words, when the signal to noise ratio in the second frame was 1, velocity correction by three times reduced the RMS error by about 18 % and this reduction happened to be approximately 50 % at SNR = 100. In fact, the less noisy the data, the closer the results to the analytical HSV. For this particular flow field, applying hierarchical PIV was not as effective as taking advantage of iteration and velocity correction at a fixed level of hierarchy.

We found out that at a fixed number of iterations, using different levels of coarsening and refining affected the RMS error depending on the value of

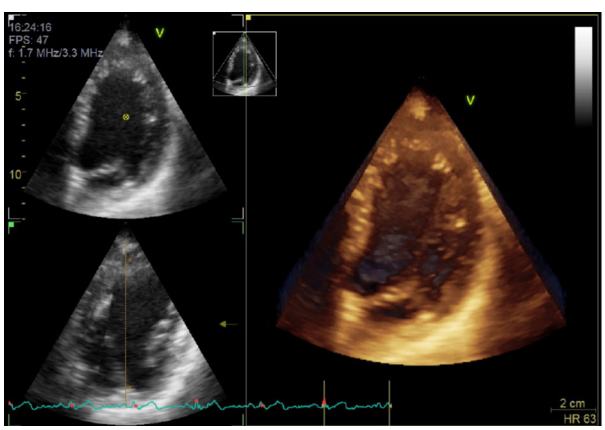

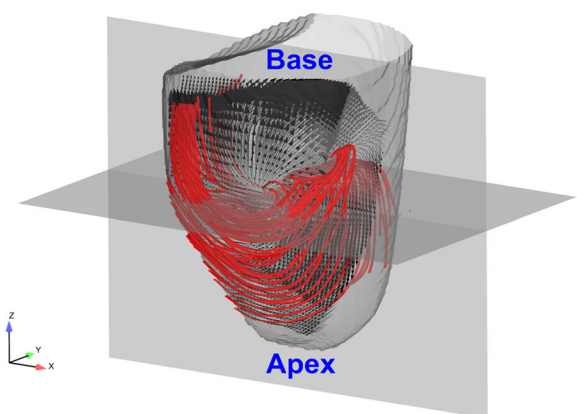

Fig. 8 (*Left*) The snapshot of the VolDICOM showing the left ventricle (LV) of the heart during early systole. Mitral valve is closed. No ultrasound contrast agent was used during the acquisition. (*Right*) The 3D velocity vector field captured by V-Echo-PIV during early systole is overlaid with the streamlines within the LV walls. For clarity purposes of streamlines, the LV is shown in a different orientation at the *right panel* compared to the *left panel*. Apex and base of the LV are also labeled. The streamlines, shown in *red*, illustrate how vortex flow, initiated during diastole, transforms into the systolic jet towards the aortic valve. (Color figure online)

SNR. At zero number of iterations, i.e., when velocity was not corrected, incorporating dataset coarsening/refining only improved the RMS error when SNR > 10. However, for SNR < 10, leveling did not enhance the RMS. When velocity was corrected once, the improvement was observed when SNR was >15. Using additional velocity corrections, the improvement was found to happen randomly due to approaching the convergency of using more iterations.

3.4 Biomechanical prospect

A recently developed volumetric echocardiographic particle image velocimetry [16] is of significant biomechanical impact in terms of studying the blood flow kinematics given the three dimensional velocity fields over the cardiac cycle, as shown in Fig. 8. Methods such as V-Echo-PIV are in continuous improvements according to both hardware and software of echocardiography systems, which necessitates the need for a systematic framework for velocimetry validation. The present study provides a synthetic validation with the broader impact in mind that ensures reliability of methods characterizing cardiovascular flow in 3D.

4 Conclusion

This study describes a framework that systematically generates a pair of 3D brightness fields interrelated according to a known 3D velocity function. This framework can be used for validating and rating the performance of different 3D PIV methods. In the present work, we used an exemplary flow field with a closed form solution (i.e., Hill's spherical vortex). Applying a known velocity function to a randomly generated brightness field (B) resulted in a second brightness field (B^*). Next the pair of (B, B^*) was independently processed to extract the velocity function that interrelated B and B^*. This velocity function was compared to the Hill's vortex' analytical velocity field for validation of the framework. The comparison found a close agreement between the computed velocity field and the analytical Hill's vortex.

Acknowledgments This study has been partially supported by an American Heart Association grant (14GRNT18800013) to Prof. Kheradvar, and a postdoctoral fellowship (14POST20530013) from the American Heart Association awarded to Dr. Falahatpisheh.

References

1. Westerweel J, Elsinga GE, Adrian RJ (2013) Particle image velocimetry for complex and turbulent flows. Annu Rev Fluid Mech 45(1):409–436
2. Pereira F, Gharib M (2002) Defocusing digital particle image velocimetry and the three-dimensional characterization of two-phase flows. Meas Sci Technol 13:683–694
3. Barnhart DH, Adrian RJ, Papen GC (1994) Phase-conjugate holographic system for high-resolution particle-image velocimetry. Appl Opt 33(30):7159–7170
4. Falahatpisheh A, Pedrizzetti G, Kheradvar A (2014) Three-dimensional reconstruction of cardiac flows based on multi-planar velocity fields. Exp Fluids 55(11):1–15
5. Elsinga GE et al (2006) Tomographic particle image velocimetry. Exp Fluids 41(6):933–947
6. Okamoto K et al (2000) Evaluation of the 3D-PIV standard images (PIV-STD project). J Vis 3(2):115–123
7. Stanislas M et al (2008) Main results of the third international PIV challenge. Exp Fluids 45(1):27–71
8. Falahatpisheh A, Kheradvar A (2012) High-speed particle image velocimetry to assess cardiac fluid dynamics in vitro: From performance to validation. Eur J Mech B Fluids 35:2–8
9. Kheradvar A, Falahatpisheh A (2012) The effects of dynamic saddle annulus and leaflet length on transmitral flow pattern and leaflet stress of a bileaflet bioprosthetic mitral valve. J Heart Valve Dis 21(2):225
10. Groves EM et al (2014) The effects of positioning of transcatheter aortic valves on fluid dynamics of the aortic root. ASAIO J 60(5):545–552
11. Sengupta PP et al (2012) Emerging trends in CV flow visualization. JACC Cardiovasc Imaging 5(3):305–316
12. Falahatpisheh A, Kheradvar A (2015) A measure of axisymmetry for vortex rings. Eur J Mech B/Fluids 49, Part A(0):264–271
13. Falahatpisheh A, Pahlevan N, Kheradvar A (2015) Effect of the mitral valve's anterior leaflet on axisymmetry of transmitral vortex ring. Ann Biomed Eng 43(10):2349–2360
14. Sánchez J, Salgado A, Monzón N (2015) Computing inverse optical flow. Pattern Recogn Lett 52:32–39
15. Norbury J (1973) A family of steady vortex rings. J Fluid Mech 57(03):417–431
16. Falahatpisheh A, Kheradvar A (2014) Volumetric echocardiographic particle image velocimetry (V-Echo-PIV). Circulation 130(Suppl 2):A14952